**This is the Pre-Published Version.**

INTERNATIONAL JOURNAL FOR NUMERICAL AND ANALYTICAL METHODS IN GEOMECHANICS
*Int. J. Numer. Anal. Meth. Geomech.* 0000; **00**:1–24
Published online in Wiley InterScience (www.interscience.wiley.com). DOI: 10.1002/nag

# A multiscale second-order work analysis approach for geotechnical structures

Hao Xiong [1,2], Zhen-Yu Yin[1*], François Nicot[2]

[1] *Department of Civil and Environmental Engineering, Hong Kong Polytechnic University, Hung Hom, Hong Kong, China.*
[2] *Universit Grenoble Alpes, Irstea, UR ETGR, Centre de Grenoble, F-38402 St-Martin dHres, France*

SUMMARY

This paper presents a second-order work analysis in application to geotechnical problems by using a novel effective multiscale approach. To abandon complicated equations involved in conventional phenomenological models, this multiscale approach employs a micromechanically-based formulation, in which only four parameters are involved. The multiscale approach makes it possible a coupling of the finite element method (FEM) and the micromechanically-based model. The FEM is used to solve the boundary value problem (BVP) while the micromechanically-based model is utilized at the Gauss point of the FEM. Then, the multiscale approach is used to simulate a three-dimensional triaxial test and a plain-strain strip footing. Based on simulations, material instabilities are analyzed at both meso and global scales. The second-order work criterion is then used to analyze the numerical results. It opens a road to interpret and understand the micro-mechanisms hiding behind the occurrence of failure in geotechnical issues. Copyright © 0000 John Wiley & Sons, Ltd.

Received ...

KEY WORDS: Granular materials, Multiscale approach, Second-order work, Micromechanics, Instability, Failure

## 1. INTRODUCTION

The geotechnical engineering problems were empirically solved until a series of theoretical advances was proposed by pioneers in soil mechanics in the early 20th century. They are well known today as bearing capacity theory (Taylor, 1948), consolidation theories (Terzaghi, 1943), limit theorem (Drucker et al., 1952; Prager, 1952). However, these theories are sometimes not suitable for real geotechnical problems due to the complexity of the problems including nonlinearities and intricate mechanisms. Since 1960s, computers and numerical tools were made accessible to geotechnical engineers. Several classes of numerical methods have been proposed to handle geotechnical engineering problems including:

(i) continuum approaches that characterize path-dependent responses with internal variables and constitutive laws on the macroscopic scale such as the finite element method (FEM) (Courant, 1943; Hrennikoff, 1941; Jin et al., 2017; Wu et al., 2017; Yin et al., 2016),

(ii) discrete approaches that explicitly introduce inter-particle contact laws among the granular assembly such as the discrete element method (DEM) (Cundall and Strack, 1979), and

*Correspondence to: Zhen-Yu Yin, Associate Professor, Department of Civil and Environmental Engineering, Hong Kong Polytechnic University, Hung Hom, Hong Kong, China. Email: zhenyu.yin@gmail.com; zhenyu.yin@polyu.edu.hk. Tel.:+852 34008470, Fax.:+852 23346389

Copyright © 0000 John Wiley & Sons, Ltd.



This is the peer reviewed version of the following article: Xiong, H, Yin, Y-Z, Nicot, F. A multiscale work-analysis approach for geotechnical structures. Int J Numer Anal Methods Geomech. 2019; 43(6): 1230–1250, which has been published in final form at https://doi.org/10.1002/nag.2893. This article may be used for non-commercial purposes in accordance with Wiley Terms and Conditions for Use of Self-Archived Versions. This article may not be enhanced, enriched or otherwise transformed into a derivative work, without express permission from Wiley or by statutory rights under applicable legislation. Copyright notices must not be removed, obscured or modified. The article must be linked to Wiley's version of record on Wiley Online Library and any embedding, framing or otherwise making available the article or pages thereof by third parties from platforms, services and websites other than Wiley Online Library must be prohibited.

(iii) multiscale approaches that build a constitutive relation on the specimen (material point) scale by taking micro-structure information into account (Chang et al., 2010; Nicot and Darve, 2011; Xiong et al., 2017; Yin et al., 2010; Yin and Chang, 2013; Yin et al., 2014).

The continuum approach has been widely used to solve geotechnical engineering problems by employing phenomenological elastoplastic models which successfully simulate the macroscopic behavior of granular assembly. Unfortunately, they do not give access to the microscopic scale in order to investigate or interpret micro-mechanisms. On the other side, the discrete approach indeed provides a simple way to do it but it is also computationally intensive to resolve the aforementioned deficiencies of continuum approaches for simulating geotechnical engineering problems.

To overcome this issue, various multiscale approaches have been proposed to couple grain-scale simulations with macroscopic continuum-scale finite element analysis. For instance, (Wellmann and Wriggers, 2012) introduced an Arlequin DEM-FEM model that divides the spatial domain into discrete and continuum sub-domains. The interaction between discrete and continuum sub-domains is assumed by overlapping with each other so that artificial reflections can be provided. (Li and Wan, 2011) proposed bridging scales methods, which uses a handshake domain to couple particulate model with higher-order continua. (Andrade et al., 2011; Guo and Zhao, 2014; Miehe et al., 2010; Nguyen et al., 2014; Nitka et al., 2011; Stránskỳ and Jirásek, 2012) proposed a conceptually similar approach where the DEM solver is used at Gauss points of the finite element mesh as a representative elementary volume (REV). Nevertheless, these DEM-FEM methods have a limitation when geotechnical engineering problems are considered due to the fact that a great number of particles need to be contained in a boundary value problem (BVP) in order to reach local convergence. It makes these methods waste computational resources resulting in inefficient simulations. Thus, micromechanically-based constitutive models should be a good alternative to couple with FEM. Among these models, the 3D-H model developed by (Xiong et al., 2017) with only four input parameters is worth trying.

On the other side, the theoretical analysis of geotechnical engineering problems is continuously progressing especially with respect to instability analysis. Many geotechnical engineering problems need to account for instability occurrence which can be classified into two main classes: flutter instabilities and divergence instabilities. The former is defined by cyclically increasing strains until failure whereas the latter leads to failure by suddenly monotonously increasing strains. If we only focus on divergence instabilities, it has been proven that for rate-independent non-associate materials, a broad domain exists, strictly within the plastic limit surface, where different failure modes can coexist (Daouadji et al., 2009; Nicot et al., 2007; Wan et al., 2013). Moreover, complicated phenomena such as strain localization and liquefaction (Hall et al., 2010; Nübel and Huang, 2004; Oda et al., 2004; Tejchman, 2004; Vardoulakis, 1996) may occur in a geotechnical problem. Since failure develops only if the second-order work vanishes or become negative along a given loading path, the second-order work is considered as a convenient criterion of failure. It is noted that the second-order work criterion does not provide a sufficient condition for failure, but the instabilities may occur with the system transforming from a quasi-static regime towards a dynamic regime when the second-order work vanishes along a given loading path (Nicot et al., 2014). This regime transformation usually relates to the occurrence of an outburst in kinetic energy, which can be detected by the vanishing of the second-order work (Nicot et al., 2017).

In this paper, the second-order work criterion is firstly reviewed. Then, an effective multiscale approach is applied to analyze geotechnical BVPs. This approach is based on a coupling between a FEM code and a micromechanically-based model (Xiong et al., 2017), where the former is used to simulate the physical domain of a BVP and the latter maintains computational efficiency while avoiding using phenomenological constitutive models at each Gauss point of the FEM. Two cases of BVPs are considered: a 3D triaxial test with fixed bottom surface and a strip footing problem. The aforementioned second-order work criterion is applied to both cases at both micro and global scales to analyze the occurrence of instability. Finally, the stress-strain (force-displacement) relations are analyzed not only on the full-scale but also at some selected Gauss points (meso-scale), highlighting the nature of failure mode.

Copyright © 0000 John Wiley & Sons, Ltd.


DOI: 10.1002/nag

## 2. SECOND-ORDER WORK CRITERION

As illustrated in (Nicot et al., 2012), the second-order work criterion has been applied to homogeneous materials under homogeneous loading conditions. It is then extended to more general conditions, where non-homogeneous stress-strain fields may develop. (Nicot et al., 2017) have proposed an approach, in which the internal and external second-order works can be computed. When no effective failure occurs, both internal and external second-order works coincide. This is advantageous as the external second-order work can be computed in a straightforward manner from the boundary variables.

Consider a material body of volume $V_0$ and density $\rho_o$ enclosed by boundary $(\Gamma_0)$ in an initial configuration $C_0$ at time $t_0$. Following a certain loading history, the body is in a strained configuration $C$ and occupies a volume $V$ of boundary $(\Gamma)$. Adopting a semi-Lagrangian formulation (each material point $\bar{x}$ of the current configuration $C$ corresponds (through bijective mapping) to a material point $\bar{X}$ of the initial configuration $C_0$), and ignoring gravity, the following equation establishes the relation between the kinetic energy of the system and the second-order work (Nguyen et al., 2016; Nicot et al., 2017):

$$\ddot{E}_c = I_2 + W_2^{ext} - W_2^{int} \tag{1}$$

where $\ddot{E}_c$ is second-order time differentiation of system kinetic energy, $I_2 = \int_{V_0} \rho_o \ddot{\bar{u}}^2 \mathrm{d}V_0$ is an inertial term, $\bar{u}(\bar{X})$ is the Lagrangian displacement field. $W_2^{ext}$ is the external second-order work, $W_2^{int}$ is the internal second-order work.

For the purpose of simplification, it is assumed hereafter that the external loading is directed by a set of components either forces $(f_i)$ or displacements $(u_i)$ applied to the boundary of the system. Thus, the external second-order work reads:

$$W_2^{ext} = \sum_{i=1}^{N} \dot{u}_i \dot{f}_i \tag{2}$$

On the other hand, the internal second-order work reads:

$$W_2^{int} = \int_{V_0} \dot{\Pi}_{ij} \dot{F}_{ij} \mathrm{d}V_0 \tag{3}$$

where $\dot{\bar{\bar{\Pi}}}$ is the first Piola-Kirchoff stress rate tensor, $\dot{\bar{\bar{F}}}$ is the velocity gradient tensor, $\dot{\bar{\bar{\Pi}}}$ and $\dot{\bar{\bar{F}}}$ are related by the constitutive relation $\dot{\Pi}_{ij} = L_{ijkl} \dot{F}_{ij}$, where the fourth-order tensor $\overset{4}{L}$ is the tangent constitutive tensor for rate-independent materials.

When the system evolves under quasi-static conditions, the inertial term $I_2$ and the kinetic energy $\ddot{E}_c$ are nil. Thus, Equation 1 yields:

$$W_2^{ext} = W_2^{int} \tag{4}$$

Equation 4 means that the internal second-order work is equal to the external second-order work when the system is quasi-static.

## 3. THE MULTISCALE APPROACH

### 3.1. A review of micromechanically-based models

In order to avoid too much sophisticated equations requiring a large number of parameters introduced by conventional phenomenological models, a micromechanically-based model is used. A couple of studies have proposed several micromechanically-based models (Chang and Hicher, 2005), among which the micro-directional model (Nicot et al., 2005) was initially proposed to describe the mechanical behavior of snow (Nicot, 2003). It was then generalized to any type of

Copyright © 0000 John Wiley & Sons, Ltd.


DOI: 10.1002/nag

granular assembly, with a particular emphasis on frictional granular materials (Nicot et al., 2005). Based on this approach, the H-directional model (the H-model for short (Nicot and Darve, 2011)) was developed in 2D conditions, replacing the notion of independent pairs of contacting particles by an intermediate granular assembly (the so-called granular hexagon, see Figure 17), in which an enriched geometrical and kinematic description can be considered. However, the granular hexagon pattern is limited to 2D conditions. Then, the H-model was extended to 3D conditions (3D-H model), replacing the 2D granular hexagons with 3D granular clusters (the so-called meso-structure, see Figure 20). This meso-structure is selected because it is large enough to contain four force chains (Tordesillas, 2007), and enable grain rearrangement. A short review of 3D-H model is given in Appendix A.

### 3.2. *Finite element formulation*

The FEM code (ABAQUS/Explicit) (Hibbitt et al., 2001) is used to solve BVPs in the context of this multiscale approach. An arbitrary geometric domain $\Omega$ of a given BVP is firstly discretized into finite element meshes with geometric position $\vec{x}$. The discretized equilibrium equation for the whole mesh reads:

$$\vec{F^e} - \vec{F^i} = \bar{\bar{M}}\vec{\ddot{u}} \tag{5}$$

where $\vec{F^e}$ is the external force vector; $\vec{F^i}$ is the internal force vector; $\bar{\bar{M}}$ is the mass matrix and $\vec{u}$ is the displacement of each material point $\vec{x}$.

In each single element $e$ of volume $V$, the internal forces reads:

$$\vec{F^i} = \int_V \vec{\sigma}(\vec{u})\bar{\bar{K}}dV = \int_V \bar{\bar{K}}^T\vec{\sigma}(\vec{u})dV \tag{6}$$

where $\bar{\bar{K}}$ is the strain-displacement rate transformation defined from the interpolation assumption as $\dot{\vec{\varepsilon}} = \bar{\bar{K}}\dot{\vec{u}}$

Thus, the dynamic equilibrium state at the current time ($t$) reads:

$$\bar{\bar{M}}\vec{\ddot{u}}|_t = (\vec{F^e} - \vec{F^i})|_t \tag{7}$$

By considering the current time $t$ and a given time increment $\Delta t$, the central difference integration scheme is used to update velocities and displacements at time $t + \frac{\Delta t}{2}$:

$$\begin{cases} \dot{\vec{u}}|_{(t+\frac{\Delta t}{2})} & = & \dot{\vec{u}}|_{(t-\frac{\Delta t}{2})} + \left(\frac{\Delta t|_{(t+\Delta t)}+\Delta t|_t}{2}\right)\ddot{\vec{u}}|_t \\ \vec{u}|_{(t+\frac{\Delta t}{2})} & = & \vec{u}|_t + \Delta t|_{(t+\Delta t)}\dot{\vec{u}}|_{(t+\frac{\Delta t}{2})} \end{cases} \tag{8}$$

The geometry is updated by adding the displacement increments to the initial geometry $\vec{x}_0$:

$$\vec{x}_{t+\Delta t} = \vec{x}_0 + \vec{u}_{t+\Delta t} \tag{9}$$

Unlike quasi-static implicit schemes, dynamic explicit schemes do not check equilibrium requirements at the end of each increment of time. The analogy between the dynamic equilibrium Equation 5 and the ideal mass-spring vibrating system allows concluding that explicit central difference time integration schemes (frequently referred as explicit integration schemes) are conditionally stable whenever the size of the time increment $\Delta t$ satisfies:

$$\Delta t \leq \frac{L_e}{E/\rho} = \frac{L_e}{c_e} \tag{10}$$

where $L_e$ is the typical size of the finite elements discretizing the domain, $E$ is the Young's modulus and $c_e$ is the velocity of a longitudinal wave in the material.

Copyright © 0000 John Wiley & Sons, Ltd.

DOI: 10.1002/nag

### 3.3. Multi-scale model implementation

The FEM implementation of the 3D-H model is part of a complete multiscale procedure. In FEM, the cell is usually called 'micro-scale' due to the fact that it is the fundamental element of a BVP. However, this cell can also be denoted 'macro-scale', because it is the finite representative elementary volume of a local homogeneous problem. To clarify, the different scales involved in this multiscale approach are depicted in Figure 1. Gauss integration points in the FEM mesh correspond to the REV scale at which the 3D-H model operates. Two intermediate scales (hexagon scale and REV scale) are introduced to bridge macro and micro scales. The element type named C3D8 (three-dimensional eight-node brick element with eight integration points) is selected. The schematic diagram of the multiscale approach is computed from macro-strain tensor to macro-stress tensor. It is assumed that the loading increment is small enough which is ensured by ABAQUS explicit solver. Note that the 3D-H model needs to store much more variables than phenomenological models require. It is therefore more computational time consuming. But the 3D-H model is much faster than discrete element method codes (or FEM×DEM codes), when a sufficiently large number of particles is used. For a time increment, the calculation process is depicted in Figure 1, and contains the following steps:

(1) A BVP domain is firstly discretized into a number of elements, each of them contains 8 Gauss integration points. The ABAQUS explicit solver is used to compute the incremental macro-strain tensor of each element based on the external loading applied on BVP. The incremental macro-strain $\delta\bar{\bar{\varepsilon}}$ is then transferred to each Gauss integration point based on the shape function of element.

(2) At each Gauss integration point, the recently developed 3D-H model (Xiong et al., 2017) is employed. For more detail derivation of 3D-H model is illustrated in Appendix A. The incremental macro-strain tensor computed from previous step is distributed to local meso-structures by using kinematic localization (Equation 17). So, the incremental deformation $\delta\vec{L}$ of meso-structure is obtained. It is worth emphasizing that the strain of each branch vector between adjoining particles of the hexagon does not derive from the macroscopic strain. In contrast, the affine assumption can reasonably be applied to describe the strain of elementary sets containing a few grains. It is analogous to the usual Voigt approximation in the field of continuous media, and has been widely used as a first approximation in granular materials (Nicot and Darve, 2011; Nicot et al., 2005; Cambou et al., 1995).

(3) Using Equation 23, the incremental forces of meso-structures are computed. So, all the contact forces and relative displacements can be solved and updated. Then, Love Weber formula (Equation 25) is used to calculate the stress tensor of each Gauss integration points, which is consequently transferred to ABAQUS explicit solver.

(4) Finally, the forces and displacements of element nodes are updated before next time increment. The time increment $dt$ is automatically estimated by ABAQUS based on the convergence of the previous time step.

### 3.4. Model parameters

A major difference between the 3D-H model and conventional phenomenological model is the number of parameters. The 3D-H model only involves four parameters: $k_n$, $k_t$, $\varphi_g$ (material parameters, introduced from contact model), and $e_0$, wherein the initial void ratio $e_0$ corresponding to the initial opening angle $\alpha_0$. A set of parameters is reported in Table I and is used in this study. This set of parameters is already calibrated to the experimental results (Xiong et al., 2017). The experiment was carried out along the conventional drained triaxial loading path with mono-disperse sand ($d_{50} = 0.6$ mm) called Ticino sand, well characterized from a geotechnical point of view and adopted in many studies (Valentino et al., 2008).

Copyright © 0000 John Wiley & Sons, Ltd.


DOI: 10.1002/nag

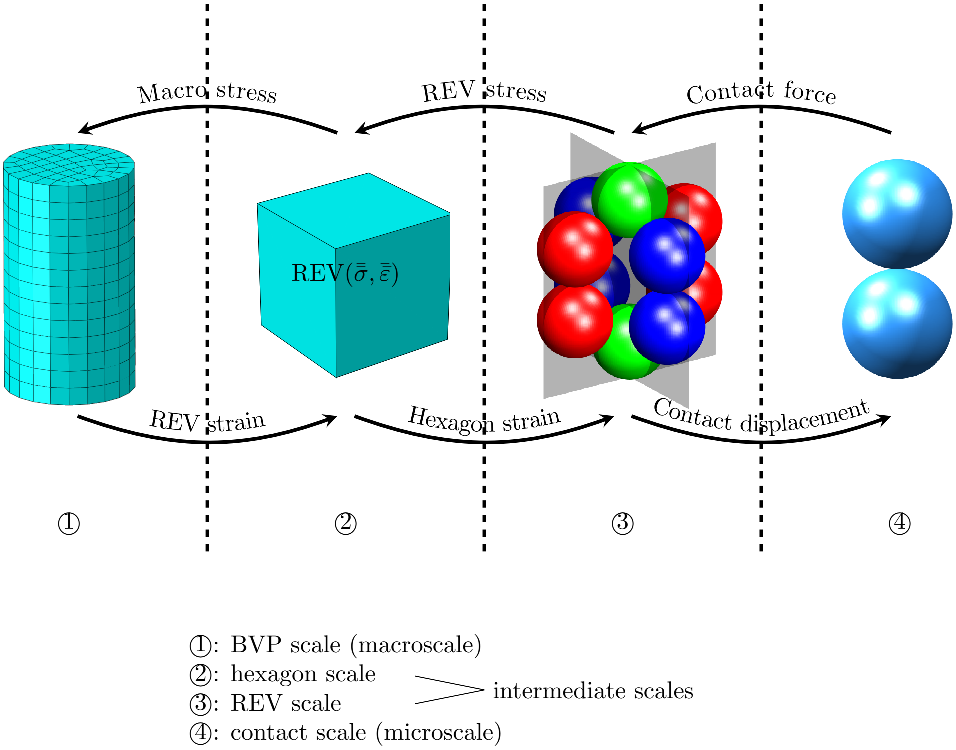


Figure 1. Interaction between scales involved in the multiscale approach.

Table I. Model parameters

| $k_n$(N/m) | $k_t/k_n$ | $e_0$ | $\varphi_g(°)$ |
|---|---|---|---|
| $1.90 \times 10^6$ | 0.6 | 0.53 | 25 |

## 4. NUMERICAL APPLICATIONS

### *4.1. Laboratory test*

Based on the multiscale approach presented in the previous section, a full three-dimensional cylindrical specimen is subjected to a drained triaxial loading path. The mesh, element type and boundary conditions are described in Figure 2. The cylinder with diameter $D = 2R$ and height $H = 4R$ is discretized into 18580 elements. The bottom surface of the specimen is permanently fixed while the confining stress $\sigma_c$ is applied to the side surface. The loading program prescribed to the specimen includes three stages: isotropically confining stage under the stress $\sigma_c$, triaxial strain control stage and triaxial stress control stage. The specimen is isotropically compressed at 200kPa during the first stage. Then, a triaxial loading path is imposed by prescribing to the top surface a constant loading speed. Finally, the loading process is switched to a stress control when the axial stress reaches a maximum value. The displacement of the top surface along direction $\vec{v_1}$ is denoted by $d_1$ while the external force is denoted by $f_1$. During the stress control, $f_1$ is imposed constant, corresponding to the maximum value of top loading at the end of the strain control stage.

Figure 3 and Figure 4 show the mechanical and volumetric responses for the 3D cylinder specimen and the deviatoric strain fields at the successive states $\varepsilon_a = 2.7\%$, $7\%$, $8\%$ and $9\%$ along a drained triaxial loading path. As shown in Figure 3, the deviatoric stress increases up to the peak (the dashed line ⊛ when $\varepsilon_a = 2.7\%$) and then decreases, with both hardening and softening regimes well reproduced. Meanwhile, the volumetric response shows a contractant behavior before $\varepsilon_a = 1\%$ and

Copyright © 0000 John Wiley & Sons, Ltd.

*Int. J. Numer. Anal. Meth. Geomech.* (0000)
DOI: 10.1002/nag

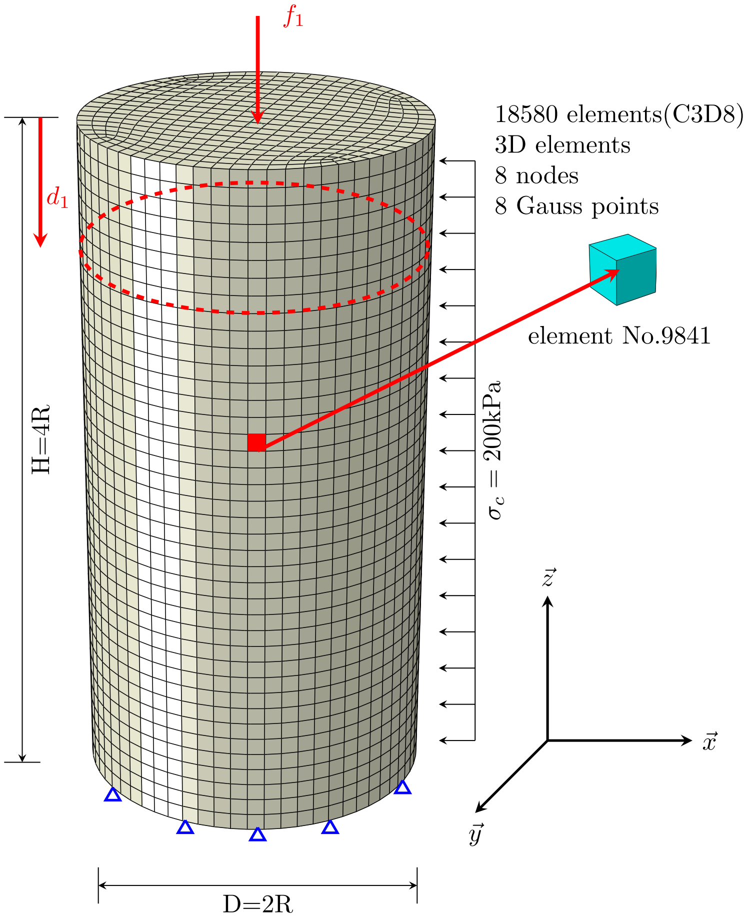


Figure 2. Mesh, element type and boundary conditions for the 3D cylinder specimen.

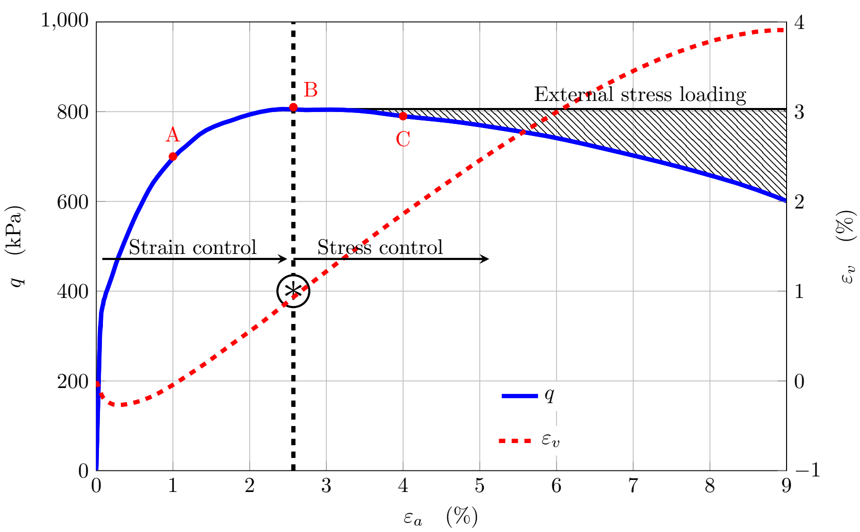


Figure 3. Mechanical and volumetric responses for a 3D cylinder specimen and strain fields at the selected states $\varepsilon_a = 2.7\%, 7\%, 8\%$ and $9\%$ along a drained triaxial loading path under a confining pressure of 200kPa.

Copyright © 0000 John Wiley & Sons, Ltd.


DOI: 10.1002/nag

a dilatant behavior after, as expected for dense sand under a drained triaxial loading path. It should be noted that the external stress loading applied to the top surface of the specimen is constant during the stress control stage. The shadow area between the deviatoric stress curve and external stress loading curve is the excess external work, which will be converted into kinetic energy of the system.

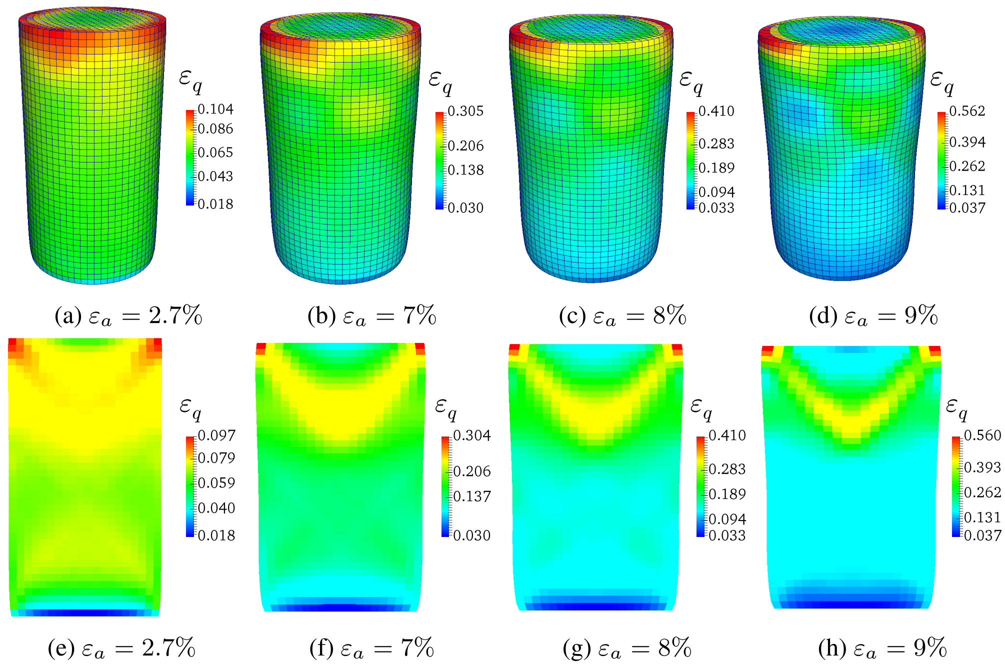


(a) $\varepsilon_a = 2.7\%$ (b) $\varepsilon_a = 7\%$ (c) $\varepsilon_a = 8\%$ (d) $\varepsilon_a = 9\%$

(e) $\varepsilon_a = 2.7\%$ (f) $\varepsilon_a = 7\%$ (g) $\varepsilon_a = 8\%$ (h) $\varepsilon_a = 9\%$

Figure 4. Deviatoric strain fields (a-d) and relevant vertical section views (e-h) at different loading states

Figure 5 reveals the microscopic variable distributions of Gauss point inside element No.9841 (shown in Figure 2) at three states corresponding to the points (A,B,C) in Figure 3.

For the sake of simplification, (a-c) shows the micro-stress integrated over $\theta$ and $\psi$ (Euler angles shown in Appendix A, Figure 19) as $\tilde{\sigma}_n^I(\varphi) = \iint \omega\tilde{\sigma}_n d\theta d\psi$; (d-f) plots the percentages of plastic meso-structures ($I_p = \frac{\text{Number of plastic contacts}}{\text{Number of total contacts}} \times 100\%$) and failure meso-structures ($I_f = \frac{\text{Number of open contacts}}{\text{Number of total contacts}} \times 100\%$) along different directions; (g-i) depicts the normalized second-order work computed as follows

$$W_{2n}^{micro}(\varphi) = \frac{\iint \frac{\delta\vec{F}\delta\vec{l}}{||\delta\vec{F}||\,||\delta\vec{l}||} d\theta d\psi}{\iint d\theta d\psi}. \tag{11}$$

In the current version of the 3D-H model, when a meso-structure fails, it is not lost, but stored in the system with no contribution. If the global deformation develops and make this opening contact re-contact, the failed meso-structure is reactivated. However, we do mention that in the current version of the model, no new local meso-structure can appear during a loading program.

The first remark is that all the micro variables show symmetrical distributions, with symmetry axes oriented along the loading direction. It should be noted that the micro-stress $\tilde{\sigma}_n^I(\varphi)$ distribution can reflect the force fabric from another side. Similarly, the plastic and failure meso-structure distributions correspond to the contact fabric. From a microscopic point of view, the 3D-H model shows properly anisotropy distributions of both fabrics for different Gauss points without involving any anisotropy parameter. For the sake of illustration, it can be observed that the magnitude of $\tilde{\sigma}_n^I(\varphi)$ in Figure 5(c) is much higher than that in Figure 5(a), but Figure 5(c) shows a narrow range. It is because a wide range of failure exists in Figure 5(f) due to the dilatant behavior (contacts open within the clusters). This failure mechanism naturally leads to the anisotropic distribution. For state

Copyright © 0000 John Wiley & Sons, Ltd.

Prepared using nagauth.cls
DOI: 10.1002/nag

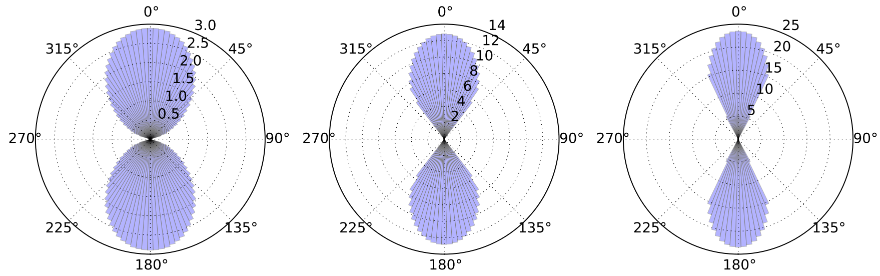

(a) $\tilde{\sigma}_n^I(\varphi)$ at state a (b) $\tilde{\sigma}_n^I(\varphi)$ at state b (c) $\tilde{\sigma}_n^I(\varphi)$ at state c

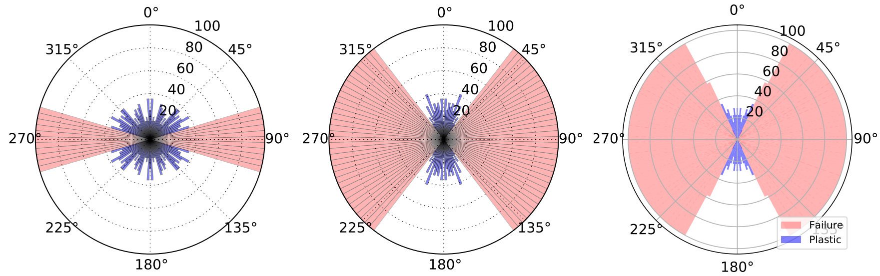


(d) $I_p$,$I_f$ at state a (e) $I_p$,$I_f$ at state b (f) $I_p$,$I_f$ at state c

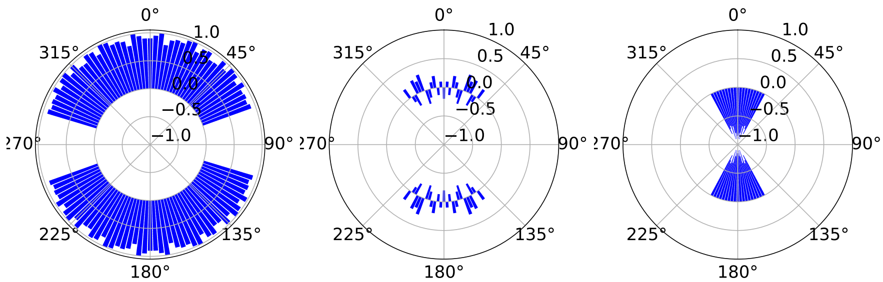

(g) $w_{2n}^{micro}(\varphi)$ at state a (h) $w_{2n}^{micro}(\varphi)$ at state b (i) $w_{2n}^{micro}(\varphi)$ at state c

Figure 5. Micro variable distributions at Gauss point in element No.9841 at the different states given in Figure 3.

a, the micro distribution of normalized second-order work is always positive, indicating that meso-structures along these directions are stable. However, as shown in Figure 5 (h), the normalized second-order work vanishes along some directions, which means that the material point has an unstable trend. Finally, the normalized second-order work along all the directions turn to be negative in Figure 5 (i).

As discussed in section 3, the external second-order work, based on the prescribed loading condition, reads:

$$W_2^{ext} = \dot{f}_1 \dot{d}_1 \tag{12}$$

In 3D conditions, the internal second-order work of the specimen is expressed as:

$$W_2^{int} = \sum_{i=1}^{n} (\dot{\bar{\bar{\sigma}}}_i : \dot{\bar{\bar{\varepsilon}}}_i) V_i \tag{13}$$

where $i$ is the element indicator, $n$ is the total number of elements, $V_i$ is the volume of the element $i$, $\sigma_i$ and $\varepsilon_i$ are stress tensor and strain tensor of element $i$, respectively.

By using Equation 12 and Equation 13, the evolution of external and internal second-order works plotted against the axial strain along the drained triaxial loading path is shown in Figure 6. It should be noted that the dashed line ⊛ is the transition from the strain control to the stress control. As

Copyright © 0000 John Wiley & Sons, Ltd.


DOI: 10.1002/nag

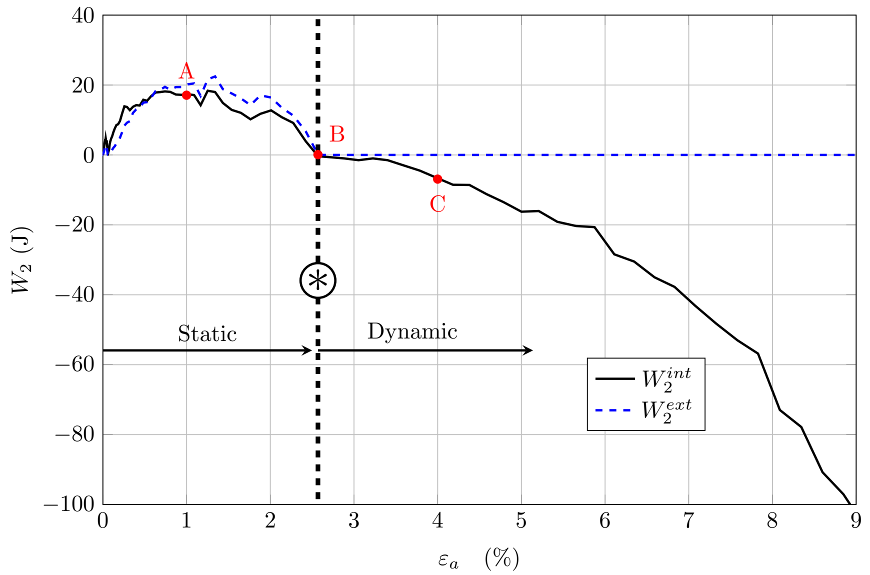


Figure 6. Evolution of external and internal second-order works versus axial strain $\varepsilon_a$ (%) for 3D cylinder specimen.

shown in Equation 1, the internal second-order work is equal to the external second-order work during the strain-controlled regime because $\ddot{E}_c$ and $I_2$ are both nil. This is verified in Figure 6 where the two curves are quite close before the dashed line $\circledast$. The very little difference between two curves is due to the fact that the loading program is not perfectly static and small inertial mechanisms can develop. As the deviatoric stress reaches the peak, the internal and external second-order works both vanish. Then, the loading method is switched to the stress control. As can be observed in Figure 6, the external second-order work after the dashed line $\circledast$ is zero as $\dot{f}_1 = 0$ (the axial force is kept constant). However, the internal second-order work is strictly negative after the dashed line $\circledast$ (the internal stress cannot balance the external loading). The difference between internal and external second-order works implies that $\ddot{E}_c$ is positive, which means that the system bifurcates from a quasi-static regime to a dynamical one. This is verified in Figure 7 where the evolution of kinetic energy of the whole system versus the axial strain is shown. The kinetic energy is close to zero during the quasi-static regime, then abruptly increases once the loading is stress controlled.

### *4.2. Geotechnical engineering problem*

The strip footing problem is an example of a non-homogeneous boundary value problem. The multiscale approach presented in section 3 is used. The mesh, element type and boundary conditions are depicted in Figure 8. For the purpose of simplification, only half of the domain is modeled due to the symmetry of the problem, and it is discretized into 56×94 elements by using the C3D8 element type. The half-domain width is $L/2 = 7.5$m and the depth is $H = 4.8$m. The half-footing width is $B/2 = 1$m. The problem is considered as a plane-strain problem. The bottom boundary is blocked in both $\vec{x}$ and $\vec{y}$ directions, whereas the left and right boundaries are only blocked in the $\vec{x}$ direction but are free to move in the $\vec{y}$ direction. The footing is modeled as a rough and rigid strip.

The loading program prescribed to the system consists of three stages. The first stage is the so-called geo-static stage, which means that the gravity is applied to the half-domain while the footing is fixed. After the initial geo-stress field is assigned to the half-domain, a displacement field is obtained. Then, the displacement field is removed after the consolidation stage. The second stage is a velocity control loading stage; the footing goes down with the vertical velocity $v_f$=0.002m/s until the third stage starts. The third stage is a force control loading stage. The vertical reaction force at the end of the second stage $R'_f$ is recorded, and is applied to the footing top surface as an external force $F^{ext}$ during the third stage.

Copyright © 0000 John Wiley & Sons, Ltd.


DOI: 10.1002/nag

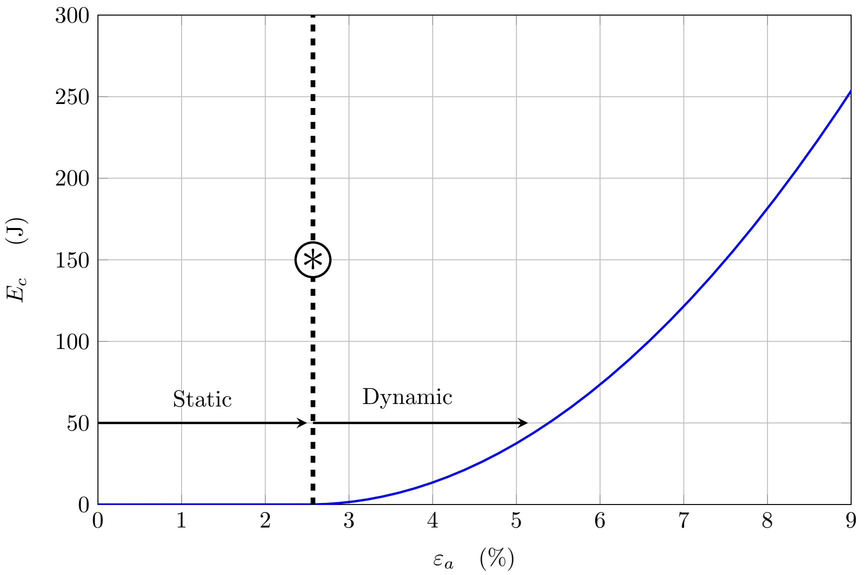


Figure 7. Evolution of kinetic energy $E_c$ (J) versus axial strain $\varepsilon_a$ (%) for the 3D cylinder specimen.

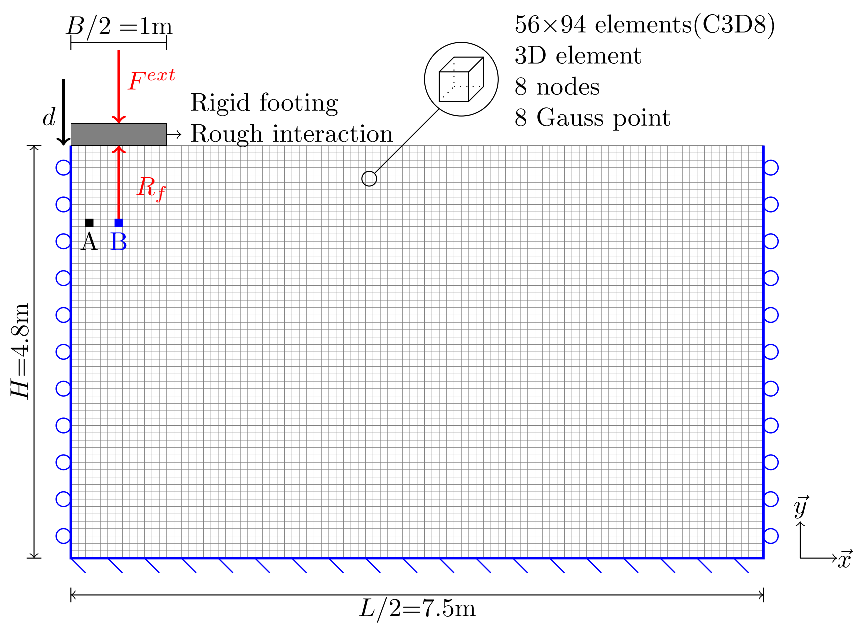


Figure 8. Mesh, element type and boundary conditions for the footing problem.

Figure 9 shows the evolution of the vertical reaction force $R_f$ versus the footing settlement $d$ (normalized by the footing width $B$). The dashed line $\circledast$ is the transition from the velocity control stage to the force control stage. As expected, the curve increases (hardening regime) before the peak and decreases after (softening regime). Figure 11 depicts the deformed meshes with distribution of plastic strain at $d/B = 1\%, 2\%, 4\%$ and $8\%$, respectively. The plastic strain initiates on the right-bottom corner of the footing and spreads to deeper zones. When $d/B = 4\%$ (the peak state in Figure 9), the plastic strain progressively localizes, but no clearly shear band can be observed. As $R_f$ goes through the peak ($d/B = 8\%$), the reaction force applied from the soil to the footing cannot accommodate the external loading due to the material softening. A triangular-shaped clod appears

Copyright © 0000 John Wiley & Sons, Ltd.

DOI: 10.1002/nag

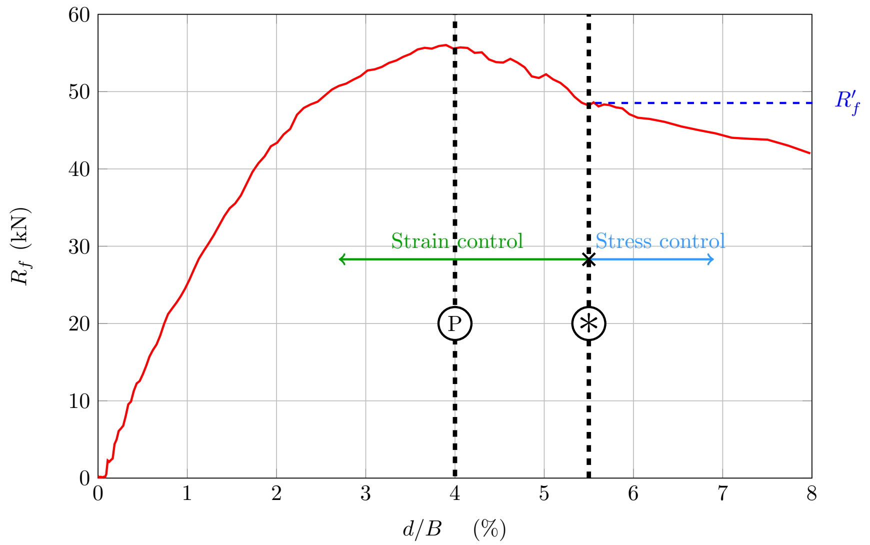


Figure 9. Evolution of the vertical reaction force $R_f$ (kN) versus the footing settlement normalized by the footing width $d/B$ (%).

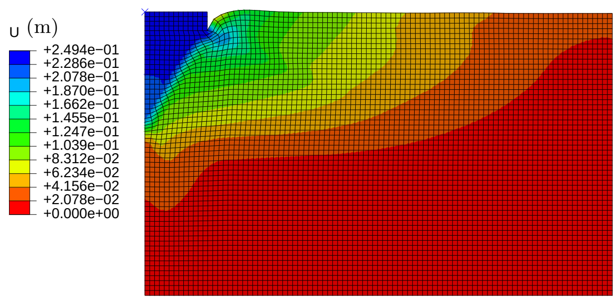


Figure 10. Displacement field at the state $d/B = 8\%$.

under the footing and an inclined shear band beneath the clod develops. Furthermore, the triangular-shaped clod can be clearly observed from the displacement field plotted in Figure 10.

According to the prescribed loading program, the external second-order work is computed from Equation 2 as:

$$W_2^{ext} = \dot{d}\dot{R}_f \tag{14}$$

As a non-homogeneous boundary value problem, the material points of the discretized system behave differently, leading to a spatial distribution of both stress and strain. The internal second-order work of the system is expressed as:

$$W_2^{int} = \sum_{i=1}^{n} (\dot{\bar{\bar{\sigma}}}_i \cdot \dot{\bar{\bar{\varepsilon}}}_i) V_i \tag{15}$$

where $i$ is the element number, $n$ is the total number of elements, $V_i$ is the volume of the element $i$.

Figure 12 gives the evolution of internal and external second-order works plotted against the normalized footing settlement. It is remarkable that the internal and external second-order works approximately coincide during the velocity-controlled loading regime ($0 < d/B < 5.5\%$). Since the velocity applied to the footing is small enough, the evolution of the system can be considered as quasi-static. According to Equation 1, the difference between internal and external second-order works is related to the inertial term $I_2$ and to the second-order time derivative of the kinetic energy

Copyright © 0000 John Wiley & Sons, Ltd.


DOI: 10.1002/nag

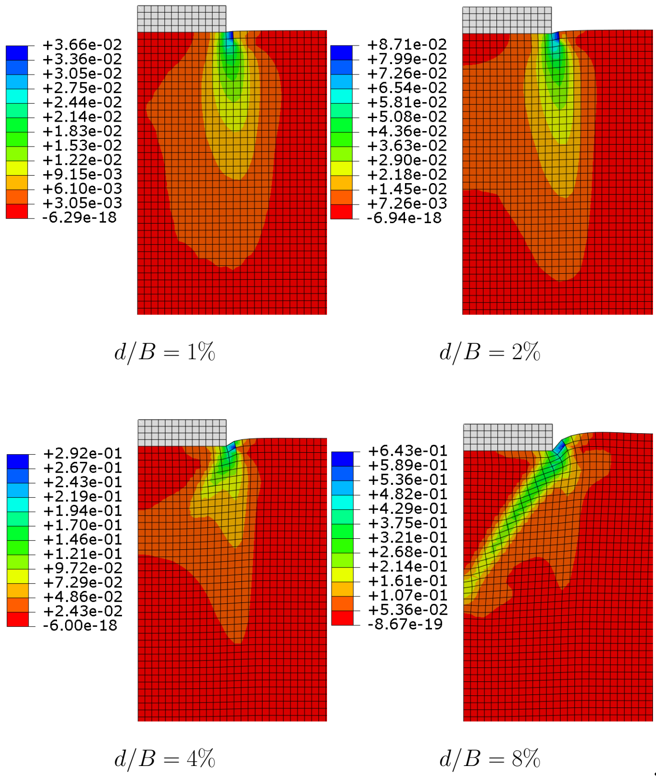


Figure 11. Deformed meshes with distribution of plastic strain $\varepsilon_p$ at different states: $d/B = 1\%, 2\%, 4\%$ and $8\%$.

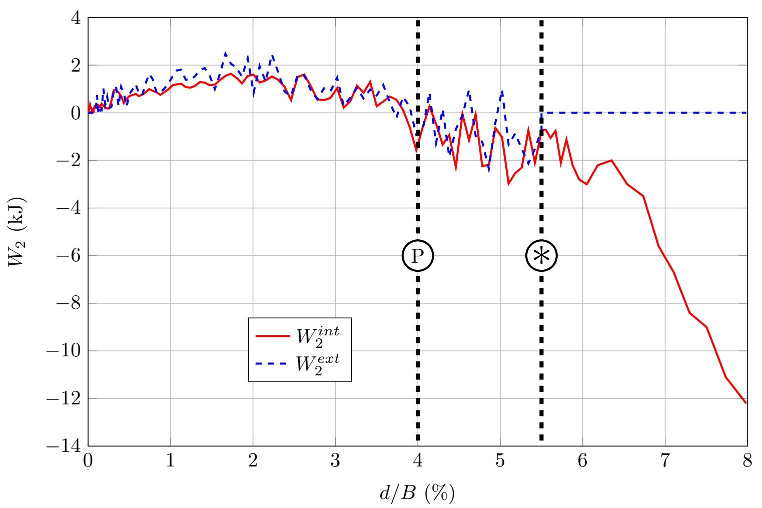


Figure 12. Evolution of internal and external second-order works versus the footing settlement normalized by the footing width $d/B$ (%).

$\ddot{E}_c$, both negligible. It is worth noting that both internal and external second-order works are positive during the first loading stage. The vanishing of the second-order work corresponds the stress peak in Figure 9 around $d/B = 4\%$. As seen in Figure 12, the two second-order work curves become more and more divergent after $d/B = 4\%$, indicating that the system is no longer stable. Especially, after the transition from velocity control to force control (dash line $\circledast$), the internal second-order work is strictly negative whereas the external second-order work equals zero as $\dot{R}_f = 0$. The difference

Copyright © 0000 John Wiley & Sons, Ltd.


DOI: 10.1002/nag

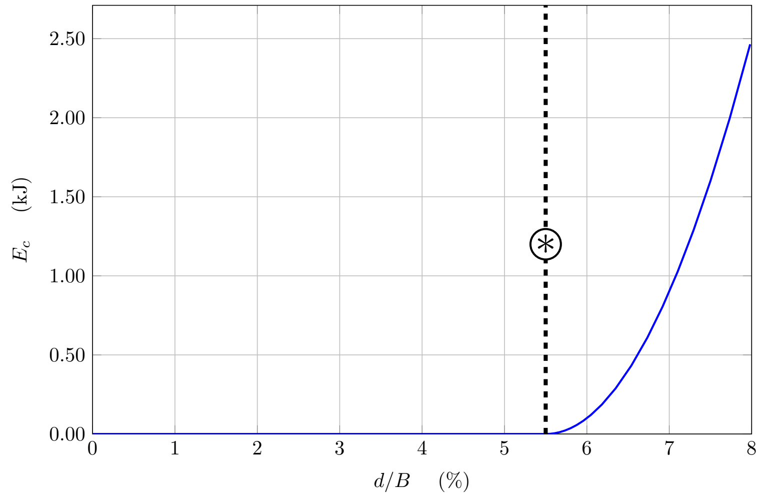


Figure 13. Evolution of kinetic energy $E_c$ (kJ) of the whole system versus the footing settlement normalized by the footing width $d/B$ (%).

301 between internal and external second-order works results in an abrupt increase in kinetic energy,
302 which is evidently observed in Figure 13.

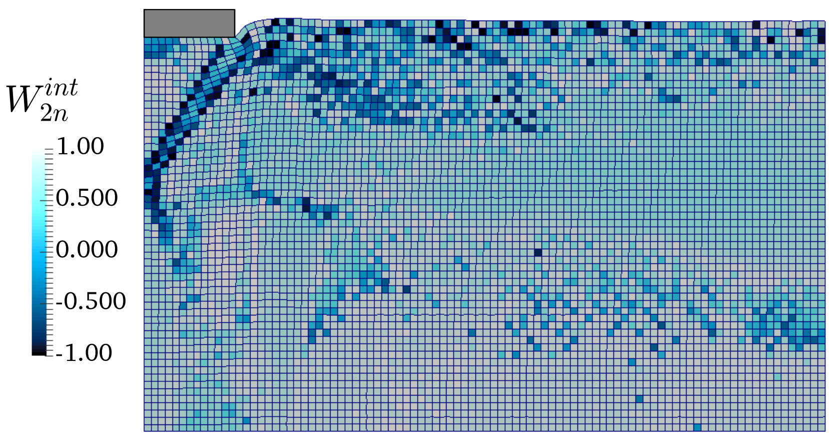


Figure 14. Deformed meshes with normalized internal second-order work distribution at the state $d/B = 8\%$.

303 For element $i$, the internal second-order work can be normalized as follows:

$$W_{2n}^{int} = \frac{\dot{\bar{\bar{\sigma}}}_i : \dot{\bar{\bar{\varepsilon}}}_i}{||\dot{\bar{\bar{\sigma}}}_i|| \cdot ||\dot{\bar{\bar{\varepsilon}}}_i||} \tag{16}$$

304 Figure 14 shows the deformed mesh with normalized internal second-order work distribution at the
305 state $d/B = 8\%$. Negative values of $W_{2n}^{int}$ mainly concentrate within two areas: A shear band area
306 below the triangular-shaped clod and a arc-shaped area in the shallow soil. The former is due to the
307 occurrence of strain localization. The mechanical response of Gauss points inside this area follows a
308 softening regime, which means that the term $\dot{\sigma}_x \dot{\varepsilon}_x$ is negative and can vanish $W_{2n}^{int}$ (see Figure 15).
309 It should be noted that significant negative values of internal second-order works concentrate at
310 the boundaries of shear bands. The latter is formed because of dilatancy behavior of the material,
311 resulting $\dot{\sigma}_y \dot{\varepsilon}_y$ to be negative.

Copyright © 0000 John Wiley & Sons, Ltd.

DOI: 10.1002/nag

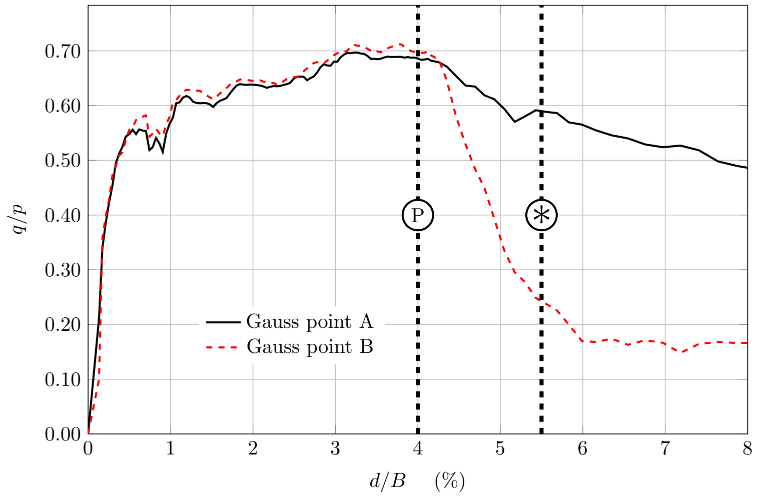


Figure 15. Evolution of deviatoric stress ratio versus normalized footing settlement corresonding to selected cells given in Figure 8.

Featuring a major advantage, the presented multiscale approach provides a straightforward way to perform both micro and meso scale analysis. The key microscopic behaviors hiding behind the macroscopic scale are helpful to understand and interpret the micro-mechanisms governing the overall response. For the purpose of demonstration, two representative cells are selected in Figure 8. They are located at the same depth to make sure that their initial states are same. Cell A locates inside the triangular-shaped clod and Cell B locates inside the shear band. Figure 15 presents the evolution of deviatoric stress ratios $q/p$ of two cells against the normalized footing settlement $d/B$. The two curves show increasing trend before $d/B = 4\%$, but decrease after that, once the material body is no longer homogeneous. It is remarkable that the peak locates on the dashed line P ($d/B = 4\%$, corresponding to the stress peak in Figure 9). The curves of cell A and B practically coincide before dashed line P, but they behave differently after that.

Figure 16 shows the micro variable distributions of cell A and cell B at two states P and *. By comparing the first column and third column of Figure 16, it can be found that the micro variable distributions of cell A and cell B are very similar at state P due to the fact that the two cells are in very close mechanical states and the macro strain is not localized yet. However, after the material undergoes softening regime, as shown in the second column and the forth column of Figure 16, the micro variable distributions of cell A and cell B are significantly different, not only because of the magnitude of $\tilde{\sigma}_n^I(\varphi)$ and $w_{2n}^{micro}(\varphi)$, but also due to the different symmetry axes. Indeed, cell B locates inside the shear band while cell A does not. Moreover, this is the reason why the internal second-order work inside shear band is negative while it is positive outside shear band (see Figure 14). Finally, these results confirm the well-recognized result that the material response and the underpinning mechanisms are totally different inside shear band area and outside shear band area (Zhu et al., 2016; Desrues et al., 1996; Vardoulakis et al., 1978; Vardoulakis, 1996).

## 5. CONCLUSIONS

This study has presented a novel effective multiscale approach to solve geotechnical boundary value problems. This multiscale approach is implemented within a FEM software to tackle the macroscopic BVPs from a micromechanically-based model to build the stress-strain relations at the Gauss points of the FEM mesh.

In order to illustrate the capability of this approach, two examples are considered with a laboratory test and a geotechnical issue. The first example presents a cylindrical specimen subjected to a drained triaxial loading path under an isotropically confining stress whereas the second example

Copyright © 0000 John Wiley & Sons, Ltd.

DOI: 10.1002/nag

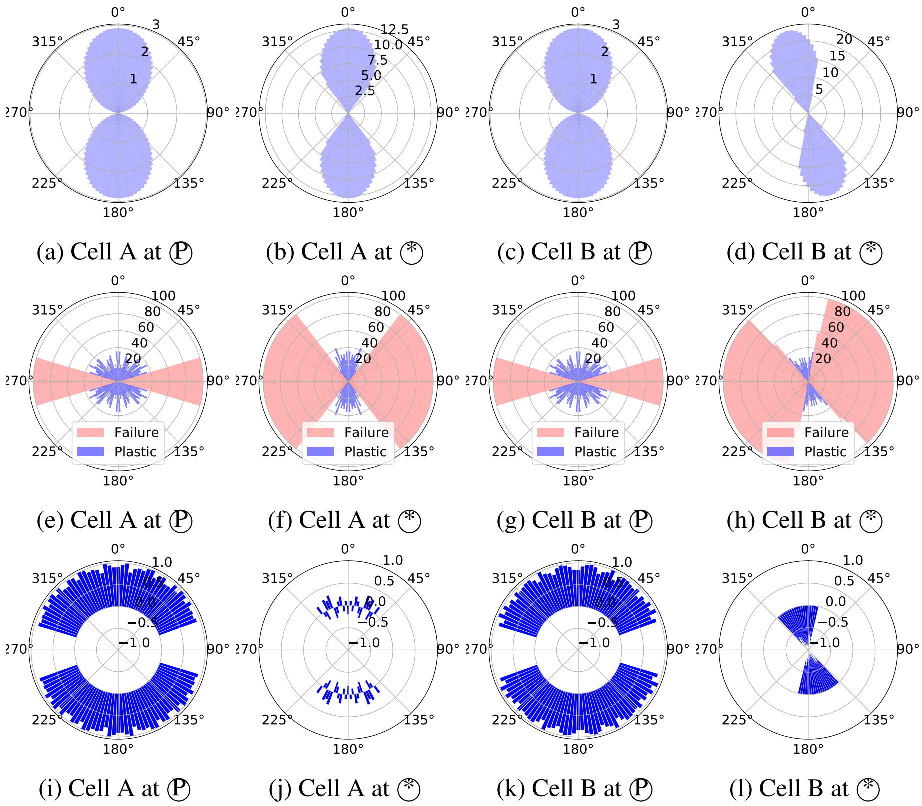


(a) Cell A at Ⓟ (b) Cell A at ⊛ (c) Cell B at Ⓟ (d) Cell B at ⊛

(e) Cell A at Ⓟ (f) Cell A at ⊛ (g) Cell B at Ⓟ (h) Cell B at ⊛

(i) Cell A at Ⓟ (j) Cell A at ⊛ (k) Cell B at Ⓟ (l) Cell B at ⊛

Figure 16. Micro variable distributions of Cell A and B (shown in Figure 8) at the states of Ⓟ and ⊛: (a-d) integrated micro-stresses ($\tilde{\sigma}_n^I(\varphi)$); (e-f) percentages of plastic and failure meso-structures ($I_p$ and $I_f$); (i-l) normalized second-order work ($w_{2n}^{micro}(\varphi)$).

illustrates a geotechnical non-homogeneous boundary value issue. From a numerical point of view, both analyses verify that when no effective failure occurs, both internal and external second-order works coincide. This is a great advantage since the external second-order can be obtained in a straightforward manner from the boundary variables without requiring internal information (internal stress or strain fields).

Furthermore, this multiscale approach utilizes an explicit-dynamic integral method so that the post-peak failure can be investigated. Thus, by switching the loading method from a strain control to a stress control at the limit state, the collapse of the system can be reflected in an abrupt increase of system kinetic energy, stemming from the difference between both internal and external second-order works.

Finally, taking advantage of the multiscale approach, the analysis can also be carried out on both the REV scale and micro-scale. The vanishing of the second-order work, as a convenient indicator of material instability, reveals a close correlation with the occurrence of strain localization. Moreover, for the sake of illustration, the micro variables distribution of cells are selected to examine local responses, illustrating the difference in the mechanical responses inside and outside shear band areas. The presented multiscale coupling model and the second-order work criterion open a road to interpret and understand the paining micromechanisms hidden behind the occurrence of failure in geotechnical issues.

Future study will focus on extending the 3D-H model. For example, the internal anisotropy can be introduced by the distribution function $\omega(\theta, \varphi, \psi)$ with an anisotropic parameter. Its evolution during shearing will be considered by modifying this anisotropic parameter with shear stress ratio, deviatoric stress, etc.

Copyright © 0000 John Wiley & Sons, Ltd.

DOI: 10.1002/nag

## A. THE DERIVATION OF 3D-H MODEL

The 3D-H model (Xiong et al., 2017) makes it possible to derive the macro-stress tensor from the macro-strain tensor according to the following steps (Figure 18):

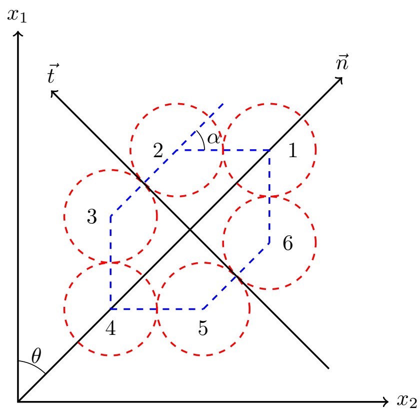


Figure 17. The 2D granular hexagon in the H-model. Angle $\alpha$ represents the elongation of the symmetric hexagon, oriented along the direction $\vec{n}(\theta)$.

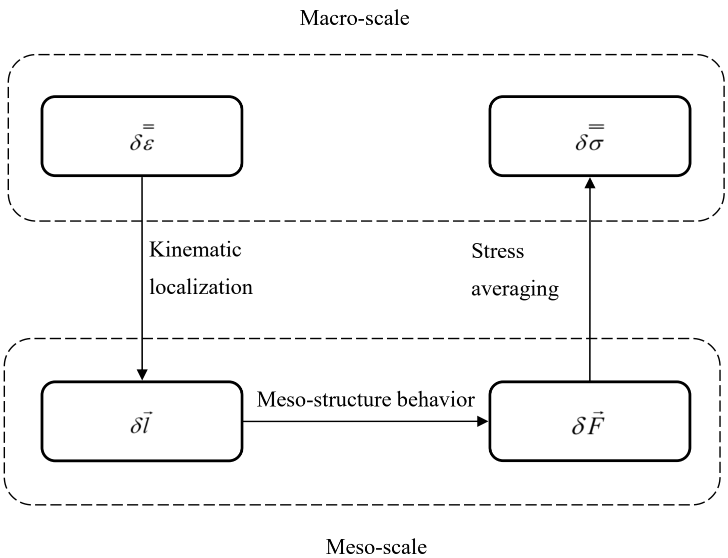


Figure 18. General homogenization scheme of 3D-H model (Cambou et al., 1995).

(1) Kinematic localization: The meso-structure is a connection between macro-scale and meso-scale. The dimension of the meso-structure can be characterized by the vector: $\vec{L} = [l_1, l_2, l_3]^T$, wherein $l_1$, $l_2$, $l_3$ represent the lengths along directions $\vec{n}$, $\vec{t}$, $\vec{w}$, respectively (see Figure 21a). Thus, the kinematic localization assumption gives:

$$\delta\vec{L} = \bar{\bar{P}}\delta\bar{\bar{\varepsilon}}\bar{\bar{P}}^{-1}\vec{L} \tag{17}$$

where: $\delta\bar{\bar{\varepsilon}}$ is the incremental macro-strain tensor, $\bar{\bar{P}}$ is the rotation matrix from global frame $(\vec{x_1}, \vec{x_2}, \vec{x_3})$ to local frame $(\vec{n}, \vec{t}, \vec{w})$ (see Figure 19).

In the 3D-H model, the strain of hexagon controlled by the vector $\delta\vec{L} = (\delta l_1, \delta l_2, \delta l_3)$ is derived from the macroscopic strain tensor. Then, the term $\delta\vec{L}$ is used as known variable to compute the

Copyright © 0000 John Wiley & Sons, Ltd.

DOI: 10.1002/nag

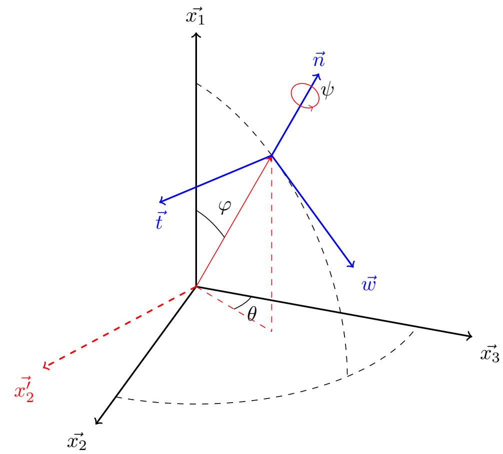


Figure 19. Global and local coordinate system transformation by employing Euler angles in 3D conditions.

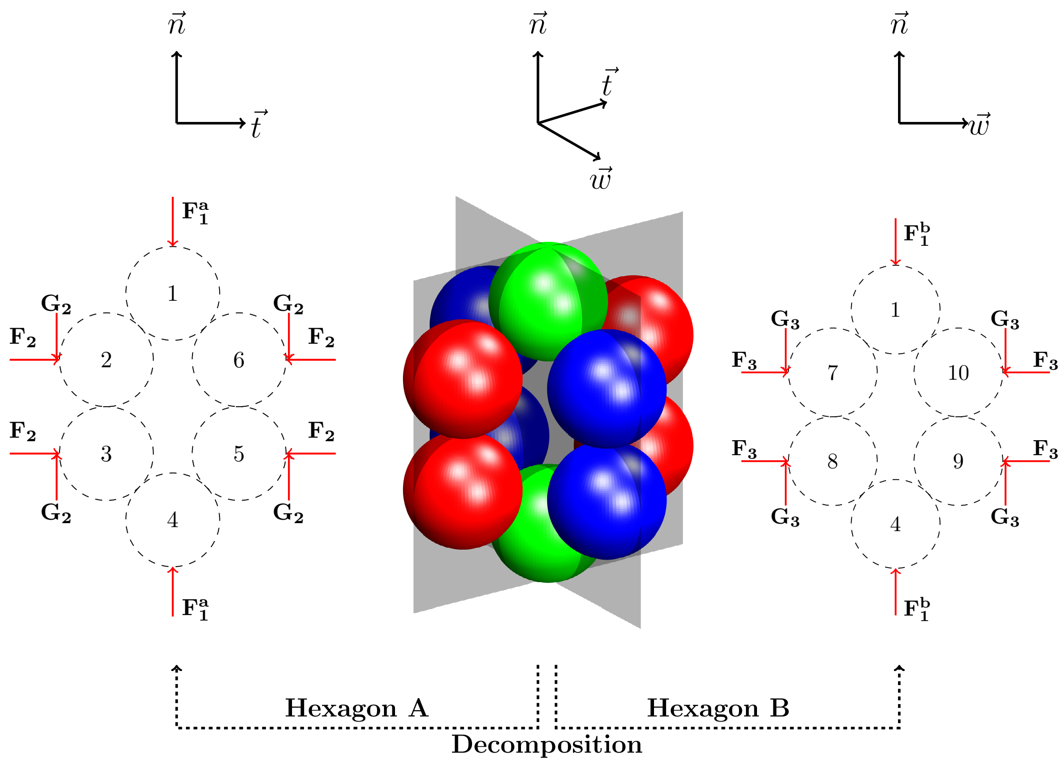


Figure 20. The 3D meso-structure and its decomposition procedure in the 3D-H model.

relative displacement of each contact and to compute contact forces. $\delta l_1, \delta l_2, \delta l_3$ are independent because there are 10 particles involved in a meso-structure, not just a single contact between particles.

(2) Meso-structure behavior: The meso-structure (Figure 20) can be decomposed into two independent hexagon patterns: Hexagon A (Figure 21) and Hexagon B (Figure 22), both being similar. The geometrical configuration and external forces applied to the meso-structure are symmetric, thus, for each hexagon, only two grains need to be analyzed. For Hexagon A, as shown in Figure 21, only grain 1 and 2 are analyzed. The contact between grain 1 and 2 is denoted by contact 1 whereas the contact between grain 2 and 3 is denoted by contact 2. Then, the kinematic

relations read (for Hexagon A):

$$\begin{aligned} \delta u_n^1 &= \delta d_1 \\ \delta u_t^1 &= d_1 \delta\alpha_1 \\ \delta u_n^2 &= \delta d_2 \end{aligned} \tag{18}$$

where $u_n^i$ and $u_t^i$ represent the normal and tangential relative displacements of contact $i$ (For Hexagon A $i = 1$ or 2, for Hexagon B $i = 3$ or 4), respectively. As depicted in Figure 21a, the geometrical descriptions for Hexagon A gives:

$$\begin{aligned} l_1 &= d_2 + 2d_1 \cos\alpha_1 \\ l_2 &= 2d_1 \sin\alpha_1 \end{aligned} \tag{19}$$

The force balance of grain 1 along direction $\vec{n}$ and of grain 2 along directions $\vec{w}$ and $\vec{n}$, together with the moment balance of grain 2 read:

$$\begin{aligned} F_1^a &= 2(N_1 \cos\alpha_1 + T_1 \sin\alpha_1) \\ F_2 &= N_1 \sin\alpha_1 - T_1 \cos\alpha_1 \\ N_2 &= N_1 \cos\alpha_1 + T_1 \sin\alpha_1 + G_2 \\ G_2 &= T_1 \end{aligned} \tag{20}$$

where $N_i$ and $T_i$ represent the normal and tangential contact forces of contact $i$, respectively. The elastic-perfect plastic inter-particle contact law reads for a given contact $i$:

$$\begin{aligned} &\delta N_i = k_n \delta u_n^i \\ &\delta\vec{T}_i = \min\left\{ \left\| \vec{T}_i + k_t \delta\vec{u}_t^i \right\|, \tan\varphi_g \left(N_i + \delta N_i\right) \right\} \times \frac{\vec{T}_i + k_t \delta\vec{u}_t^i}{\left\| \vec{T}_i + k_t \delta\vec{u}_t^i \right\|} - \vec{T}_i \end{aligned} \tag{21}$$

After simplifying (see more details in Appendix B), the contact law (for Hexagon A) can be rewritten as follows:

$$\begin{aligned} \delta N_1 &= -k_n \delta d_1 \\ \delta N_2 &= -k_n \delta d_2 \\ \delta T_1 &= B_1 \delta\alpha_1 - A_1 \delta d_1 + C_1 \end{aligned} \tag{22}$$

For the purpose of simplification, term $C_1$ is negligible. It differs from zero only during a transition from elastic regime to plastic regime. Except this situation, it is zero. For very small strain increments, as considered throughout this paper, term $C_1$ can therefore be neglected.

It should be noted that there are 14 unknowns among 12 equations (Equations (18), (20) and (22)). Thus, for Hexagon A, a two-order algebraic relation between $(\delta F_1^a, \delta F_2)$ and $(\delta l_1, \delta l_2)$ can be expressed as follows:

$$\frac{1}{|D|^a} \begin{bmatrix} K_{11}^a & K_{12}^a \\ K_{21}^a & K_{22}^a \end{bmatrix} \begin{bmatrix} \delta l_1 \\ \delta l_2 \end{bmatrix} = \begin{bmatrix} \delta F_1^a \\ \delta F_2 \end{bmatrix} \tag{23}$$

where:

$$\left\{ \begin{array}{lcl} K_{11}^a & = & 2\left(F_2 \sin\alpha_1 - k_n d_1 \cos^2\alpha_1 - k_t d_1 \sin^2\alpha_1\right) \\ K_{12}^a & = & \left(k_t d_1 \sin\alpha_1 - F_2\right)\left(\frac{A_1}{k_n}\sin\alpha_1 + \frac{A_1}{k_n} + 3\cos\alpha_1\right) \\ & & -\cos\alpha_1\left(B_1 \sin\alpha_1 + B_1 - F_2 + 2k_n d_1 \sin\alpha_1\right) \\ K_{21}^a & = & 2\left(k_t - k_n\right) d_1 \sin\alpha_1 \cos\alpha_1 - 2F_1^a \sin\alpha_1 \\ K_{22}^a & = & \left(F_1^a - k_t d_1 \cos\alpha_1\right)\left(\frac{A_1}{k_n}\sin\alpha_1 + \frac{A_1}{k_n} + 3\cos\alpha_1\right) \\ & & -\sin\alpha_1\left(B_1 \sin\alpha_1 + B_1 - F_2 + 2k_n d_1 \sin\alpha_1\right) \\ |D|^a & = & \frac{2}{k_n}(B_1 \sin\alpha_1 + A_1 d_1 \cos\alpha_1)(\sin\alpha_1 + 1) \\ & & -\frac{2}{k_n}(F_2 \sin\alpha_1 + k_n d_1 \cos^2\alpha_1 + 2k_n d_1) \end{array} \right. \tag{24}$$

Similarly, the incremental constitutive relation for Hexagon B can also be obtained. Consequently, superimposing Hexagon A and Hexagon B, the total incremental force along direction $\vec{n}$ is $\delta\vec{F}_1 = \delta\vec{F}_1^a + \delta\vec{F}_1^b$. The incremental constitutive relation of the 3D meso-structure is finally obtained.

Copyright © 0000 John Wiley & Sons, Ltd.

DOI: 10.1002/nag

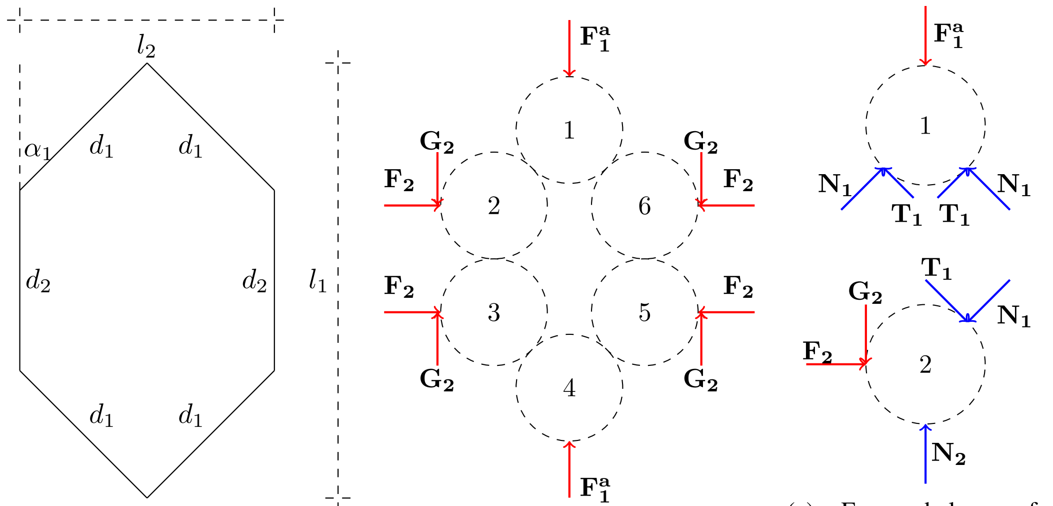


(a) Dimension of Hexagon A (b) External forces (c) Force balance for grains 1 and 2

Figure 21. Mechanical description of Hexagon A.

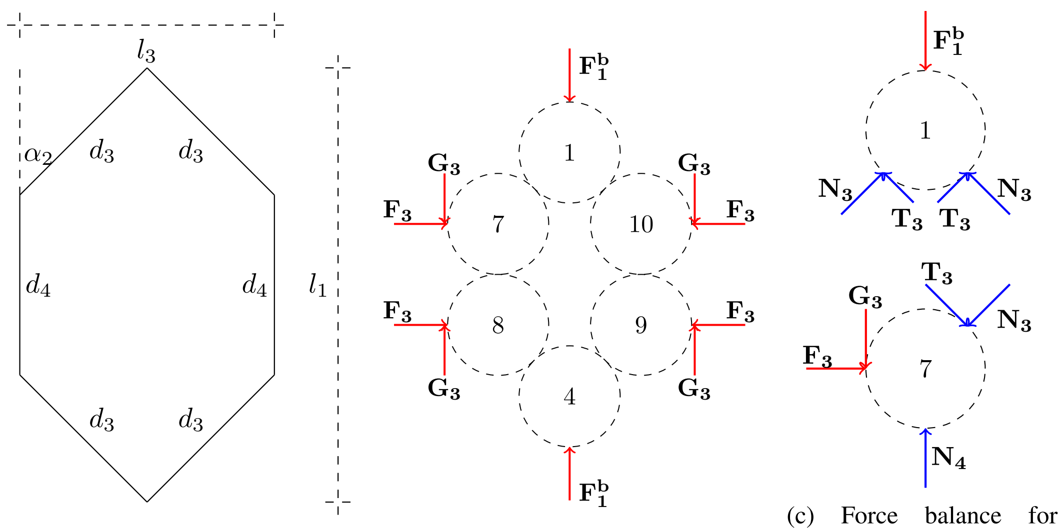


(a) Dimension of Hexagon B (b) External forces (c) Force balance for grains 1 and 7

Figure 22. Mechanical description of Hexagon B.

(3) Stress averaging: Averaging the meso-stress $\bar{\bar{\tilde{\sigma}}}$ taking place within all the meso-structures in the specimen of volume $V$ can be performed as follows:

$$\bar{\bar{\sigma}} = \frac{1}{V}\iiint \omega(\theta,\varphi,\psi)\bar{\bar{P}}^{-1}\bar{\bar{\tilde{\sigma}}}(\vec{n},\vec{t},\vec{w})\bar{\bar{P}}\sin\varphi d\varphi d\theta d\psi \tag{25}$$

where $\bar{\bar{\sigma}}$ is the macro-stress tensor operating on the specimen scale. For an isotropic specimen, the distribution function $\omega(\theta,\varphi,\psi)$ is uniform with $\theta\in[0,2\pi[$, $\varphi\in[0,\pi]$, $\psi\in[0,2\pi[$ ($\theta,\varphi,\psi$ are the Euler angles). The meso-stress $\bar{\bar{\tilde{\sigma}}}(\vec{n},\vec{t},\vec{w})$ with respect to the local frame can be computed from the

Copyright © 0000 John Wiley & Sons, Ltd.

DOI: 10.1002/nag

local variables (Figure 21 and Figure 22) by using the Love-Weber formula (De Saxcé et al., 2004; Love, 2013; Christoffersen et al., 1981; Mehrabadi et al., 1982):

$$\begin{array}{rcl}\widetilde{\sigma}_{11}(\vec{n},\vec{t},\vec{w}) & = & 4N_1 d_1 \cos^2\alpha_1 + 4T_1 d_1 \cos\alpha_1 \sin\alpha_1 + 2N_2 d_2 \\ & & +4N_3 d_3 \cos^2\alpha_2 + 4T_3 d_3 \cos\alpha_2 \sin\alpha_2 + 2N_4 d_4 \\ \widetilde{\sigma}_{22}(\vec{n},\vec{t},\vec{w}) & = & 4N_1 d_1 \sin^2\alpha_1 - 4T_1 d_1 \cos\alpha_1 \sin\alpha_1 \\ \widetilde{\sigma}_{33}(\vec{n},\vec{t},\vec{w}) & = & 4N_3 d_3 \sin^2\alpha_2 - 4T_3 d_3 \cos\alpha_2 \sin\alpha_2 \\ \widetilde{\sigma}_{ij}(\vec{n},\vec{t},\vec{w}) & = & 0 \quad \text{when} \quad i \neq j \end{array} \tag{26}$$

The principal components of meso-stress tensor are calculated from the internal forces acting within the meso-structure. Besides, off-diagonal components can be simply considered as nil, because the meso-structure with respect to $(\vec{n},\vec{t},\vec{w})$ always offsets the one with respect to $(-\vec{n},-\vec{t},-\vec{w})$ in off-diagonal components when integrated.

It is worth noting that the local void ratio is related to the opening angle, which is not related to local anisotropy. The opening angle $\alpha_{1(2)}$ is only a geometrical parameter, and can be found in Figure 21 and Figure 22. The opening angle, together with the components $l_1, l_2, l_3$, determine the initial shape of the hexagons, and thus determines the local void ratio of the meso-structure.

## B. CONTACT LAW

This elastic-perfect plastic model includes a Mohr-Coulomb criterion and can be expressed under the following incremental formalism:

$$\left\{\begin{array}{l}\delta N_i = k_n \delta u_n^i \\ \delta T_i = \min\left\{\left\|T_i + k_t \delta u_t^i\right\|, \tan\varphi_g\left(N_i + k_n \delta u_n^i\right)\right\} \times \frac{T_i + k_t \delta u_t^i}{\left\|T_i + k_t \delta u_t^i\right\|} - T_i\end{array}\right. \tag{27}$$

where: $i = 1, 2, 3, 4$ denotes the identifier of contact number.

According to Equations 18, Equations 27 can be rewritten as follows:

$$\left\{\begin{array}{ll}\delta N_i = -k_n \delta d_i & \\ \delta T_i = k_t d_i \delta\alpha_j & \text{elastic regime} \\ \delta T_i = \tan\varphi_g\left(N_i - k_n \delta d_i\right)\xi_i - T_i & \text{plastic regime}\end{array}\right. \tag{28}$$

where: $\xi_i$ is the sign of $T_i + k_t d_i \delta\alpha_j$; $j = 1$ when $i = 1, 2$; $j = 2$ when $i = 3, 4$; plastic regime is reached when $\| k_t d_i \delta\alpha_j + T_i \| \geqslant \tan\varphi_g\left(N_i - k_n \delta d_i\right)$, otherwise it is in elastic regime.

To facilitate the derivation, $I_i^p$ and $I_i^e$ are introduced as indicator functions of the contact state, expressed as follow:

$$I_i^p = \left\{\begin{array}{ll}1 & \text{in plastic regime} \\ 0 & \text{in elastic regime}\end{array}\right. \quad ; \quad I_i^e = 1 - I_i^p \tag{29}$$

Thus, the constitutive relations can be expressed as:

$$\left\{\begin{array}{l}\delta N_i = -k_n \delta d_i \\ \delta T_i = B_i \delta\alpha_j - A_i \delta d_i + C_i\end{array}\right. \tag{30}$$

where: $\left\{\begin{array}{l}A_i = I_i^p k_n \xi_i \tan\varphi_g \\ B_i = I_i^e k_t d_i \\ C_i = I_i^p\left(\xi_i \tan\varphi_g N_i - T_i\right)\end{array}\right.$

## REFERENCES

Andrade, J.E., Avila, C., Hall, S., Lenoir, N., Viggiani, G., 2011. Multiscale modeling and characterization of granular matter: from grain kinematics to continuum mechanics. Journal of the Mechanics and Physics of Solids 59, 237–250.

Copyright © 0000 John Wiley & Sons, Ltd.

DOI: 10.1002/nag

Cambou, B., Dubujet, P., Emeriault, F., Sidoroff, F., 1995. Homogenization for granular materials. European journal of mechanics. A. Solids 14, 255–276.

Chang, C., Hicher, P.Y., 2005. An elasto-plastic model for granular materials with microstructural consideration. International journal of solids and structures 42, 4258–4277.

Chang, C., Yin, Z.Y., Hicher, P.Y., 2010. Micromechanical analysis for interparticle and assembly instability of sand. Journal of Engineering Mechanics 137, 155–168.

Christoffersen, J., Mehrabadi, M.M., Nemat-Nasser, S., 1981. A micromechanical description of granular material behavior. Journal of Applied Mechanics 48, 339–344.

Courant, R., 1943. Variational methods for the solution of problems of equilibrium and vibrations. Bulletin of the American mathematical Society 49, 1–23.

Cundall, P.A., Strack, O.D., 1979. A discrete numerical model for granular assemblies. geotechnique 29, 47–65.

Daouadji, A., AlGali, H., Darve, F., Zeghloul, A., 2009. Instability in granular materials: experimental evidence of diffuse mode of failure for loose sands. Journal of Engineering Mechanics 136, 575–588.

De Saxcé, G., Fortin, J., Millet, O., 2004. About the numerical simulation of the dynamics of granular media and the definition of the mean stress tensor. Mechanics of Materials 36, 1175–1184.

Desrues, J., Chambon, R., Mokni, M., Mazerolle, F., 1996. Void ratio evolution inside shear bands in triaxial sand specimens studied by computed tomography. Géotechnique 46, 529–546.

Drucker, D., Prager, W., Greenberg, H., 1952. Extended limit design theorems for continuous media. Quarterly of Applied Mathematics 9, 381–389.

Guo, N., Zhao, J., 2014. A coupled fem/dem approach for hierarchical multiscale modelling of granular media. International journal for numerical methods in engineering 99, 789–818.

Hall, S., Bornert, M., Desrues, J., Pannier, Y., Lenoir, N., Viggiani, G., Bésuelle, P., 2010. Discrete and continuum analysis of localised deformation in sand using x-ray $\mu$ct and volumetric digital image correlation. Géotechnique 60, 315–322.

Hibbitt, Karlsson, Sorensen, 2001. ABAQUS/Explicit: User's Manual. volume 1. Hibbitt, Karlsson and Sorenson Incorporated.

Hrennikoff, A., 1941. Solution of problems of elasticity by the framework method. Journal of applied mechanics 8, 169–175.

Jin, Y.F., Wu, Z.X., Yin, Z.Y., Shen, J.S., 2017. Estimation of critical state-related formula in advanced constitutive modeling of granular material. Acta Geotechnica 12, 1329–1351.

Li, X., Wan, K., 2011. A bridging scale method for granular materials with discrete particle assembly–cosserat continuum modeling. Computers and Geotechnics 38, 1052–1068.

Love, A.E.H., 2013. A treatise on the mathematical theory of elasticity. volume 1. Cambridge University Press.

Mehrabadi, M.M., Nemat-Nasser, S., Oda, M., 1982. On statistical description of stress and fabric in granular materials. International Journal for Numerical and Analytical Methods in Geomechanics 6, 95–108.

Miehe, C., Dettmar, J., Zäh, D., 2010. Homogenization and two-scale simulations of granular materials for different microstructural constraints. International Journal for Numerical Methods in Engineering 83, 1206–1236.

Copyright © 0000 John Wiley & Sons, Ltd.
*Prepared using* nagauth.cls

Nguyen, H.N., Prunier, F., Djeran-Maigre, I., Nicot, F., 2016. Kinetic energy and collapse of granular materials. Granular Matter 18, 1–10.

Nguyen, T., Combe, G., Caillerie, D., Desrues, J., 2014. Fem× dem modelling of cohesive granular materials: numerical homogenisation and multi-scale simulations. Acta Geophysica 62, 1109–1126.

Nicot, F., 2003. Constitutive modelling of a snow cover with a change in scale. European Journal of Mechanics-A/Solids 22, 325–340.

Nicot, F., Darve, F., 2011. The H-microdirectional model: accounting for a mesoscopic scale. Mechanics of Materials 43, 918–929.

Nicot, F., Darve, F., Group, R., 2005. A multi-scale approach to granular materials. Mechanics of materials 37, 980–1006.

Nicot, F., Hadda, N., Sibille, L., Radjai, F., Hicher, P.Y., Darve, F., 2014. Some micromechanical aspects of failure in granular materials based on second-order work. Comptes Rendus Mécanique 342, 174–188.

Nicot, F., Lerbet, J., Darve, F., 2017. Second-order work criterion: from material point to boundary value problems. Acta Mechanica , 1–16.

Nicot, F., Sibille, L., Darve, F., 2012. Failure in rate-independent granular materials as a bifurcation toward a dynamic regime. International Journal of Plasticity 29, 136–154.

Nicot, F., Sibille, L., Donze, F., Darve, F., 2007. From microscopic to macroscopic second-order work in granular assemblies. Mechanics of materials 39, 664–684.

Nitka, M., Combe, G., Dascalu, C., Desrues, J., 2011. Two-scale modeling of granular materials: a dem-fem approach. Granular Matter 13, 277–281.

Nübel, K., Huang, W., 2004. A study of localized deformation pattern in granular media. Computer Methods in Applied Mechanics and Engineering 193, 2719–2743.

Oda, M., Takemura, T., Takahashi, M., 2004. Microstructure in shear band observed by microfocus x-ray computed tomography. Geotechnique 54, 539–542.

Prager, W., 1952. The general theory of limit design, in: Proceedings of the 8th International Congress on theoretical and Applied Mechanics, Istanbul, pp. 65–72.

Stránskỳ, J., Jirásek, M., 2012. Open source fem-dem coupling. Engineering Mechanics , 18.

Taylor, D.W., 1948. Fundamentals of soil mechanics.. volume 66. Wiley: New York.

Tejchman, J., 2004. Fe-analysis of patterning of shear zones in granular bodies for earth pressure problems of a retaining wall. Archives of Hydro-Engineering and Environmental Mechanics 51, 317–348.

Terzaghi, K., 1943. Theory of consolidation. Wiley: New York.

Tordesillas, A., 2007. Force chain buckling, unjamming transitions and shear banding in dense granular assemblies. Philosophical Magazine 87, 4987–5016.

Valentino, R., Barla, G., Montrasio, L., 2008. Experimental analysis and micromechanical modelling of dry granular flow and impacts in laboratory flume tests. Rock Mechanics and Rock Engineering 41, 153.

Vardoulakis, I., 1996. Deformation of water-saturated sand: I. uniform undrained deformation and shear banding. Géotechnique 46, 441–456.

Copyright © 0000 John Wiley & Sons, Ltd.


DOI: 10.1002/nag

Vardoulakis, I., Goldscheider, M., Gudehus, G., 1978. Formation of shear bands in sand bodies as a bifurcation problem. International Journal for numerical and analytical methods in Geomechanics 2, 99–128.

Wan, R., Pinheiro, M., Daouadji, A., Jrad, M., Darve, F., 2013. Diffuse instabilities with transition to localization in loose granular materials. International Journal for Numerical and Analytical Methods in Geomechanics 37, 1292–1311.

Wellmann, C., Wriggers, P., 2012. A two-scale model of granular materials. Computer Methods in Applied Mechanics and Engineering 205, 46–58.

Wu, Z.X., Yin, Z.Y., Jin, Y.F., Geng, X.Y., 2017. A straightforward procedure of parameters determination for sand: a bridge from critical state based constitutive modelling to finite element analysis. European Journal of Environmental and Civil Engineering , 1–23.

Xiong, H., Nicot, F., Yin, Z., 2017. A three-dimensional micromechanically based model. International Journal for Numerical and Analytical Methods in Geomechanics .

Yin, Z.Y., Chang, C.S., 2013. Stress–dilatancy behavior for sand under loading and unloading conditions. International Journal for Numerical and Analytical Methods in Geomechanics 37, 855–870.

Yin, Z.Y., Chang, C.S., Hicher, P.Y., 2010. Micromechanical modelling for effect of inherent anisotropy on cyclic behaviour of sand. International Journal of Solids and Structures 47, 1933–1951.

Yin, Z.Y., Hicher, P.Y., Dano, C., Jin, Y.F., 2016. Modeling mechanical behavior of very coarse granular materials. Journal of Engineering Mechanics 143, C4016006.

Yin, Z.Y., Zhao, J., Hicher, P.Y., 2014. A micromechanics-based model for sand-silt mixtures. International journal of solids and structures 51, 1350–1363.

Zhu, H., Nguyen, H.N., Nicot, F., Darve, F., 2016. On a common critical state in localized and diffuse failure modes. Journal of the Mechanics and Physics of Solids 95, 112–131.

Copyright © 0000 John Wiley & Sons, Ltd.

*Prepared using* nagauth.cls
DOI: 10.1002/nag